

Graphene Oxide–IPDI–Ag/ZnO@Hydroxypropyl Cellulose Nanocomposite Films for Biological Wound-Dressing Applications

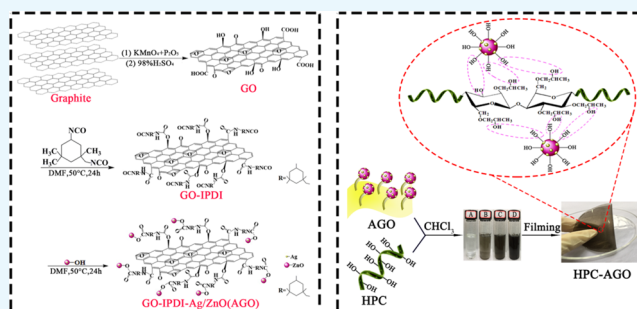
Yiwei Wang,^{†,||} Liujuan Shi,^{†,||} Haoping Wu,[‡] Qingyang Li,[§] Wei Hu,[‡] Zhenbao Zhang,[‡] Langhuan Huang,[‡] Jingxian Zhang,[‡] Dengjie Chen,[‡] Suiping Deng,[‡] Shaozao Tan,^{*,‡,||} and Zhenyou Jiang^{*,†}

[†]Department of Microbiology and Immunology, School of Medicine, Jinan University, Guangzhou 510632, China

[‡]Guangdong Engineering & Technology Research Centre of Graphene-Like Materials and Products, Department of Chemistry, College of Chemistry and Materials Science, Jinan University, Guangzhou 510632, China

[§]Institute of Clinical Oncology of Jinan University, The First Affiliated Hospital of Jinan University, Guangzhou, Guangdong 510630, China

ABSTRACT: In this work, we proposed a feasible approach to prepare multifunctional composite films by introducing a nanoscaled filler into a polymer matrix. Specifically, thanks to isophorone diisocyanate (IPDI) acting as a coupling agent, the hydroxyl groups and carboxyl groups on the surface of graphene oxide (GO) and the hydroxyl groups on the surface of silver-coated zinc oxide nanoparticles (Ag/ZnO) are covalently grafted, forming GO–IPDI–Ag/ZnO (AGO). The prepared AGO was then introduced into the hydroxypropyl cellulose (HPC) matrix to form AGO@HPC nanocomposite films by solution blending. AGO@HPC nanocomposite films exhibited improved mechanical, anti-ultraviolet, and antibacterial properties. Specifically, a tensile test showed that the tensile strength of the prepared AGO@HPC nanocomposite film with the addition of as low as 0.5 wt % AGO was increased by about 16.2% compared with that of the pure HPC film. In addition, AGO@HPC nanocomposite films showed a strong ultraviolet resistance and could effectively inactivate both Gram-negative (*Escherichia coli*) and Gram-positive (*Staphylococcus aureus*) bacteria at a low loading of AGO, and rapid sterilization plays a crucial role in wound-healing. In vivo results show that the AGO@HPC release of Ag⁺ and Zn²⁺ stimulates the immune function to produce a large number of white blood cells and neutrophils, thereby producing the synergistic antibacterial effects and accelerated wound-healing. Therefore, our results suggest that these novel AGO@HPC nanocomposite films with improved mechanical, anti-ultraviolet, and antibacterial properties could be promising candidates for antibacterial packaging, biological wound-dressing, etc. The abuse of antibiotics has brought about serious drug-resistant bacteria, and our nanofilm antibacterial does not entail such problems. In addition, local administration reduces the possibility of changing the body's immune system and organ toxicity, which greatly increases the safety.



1. INTRODUCTION

Nowadays, nonrenewable natural resources such as petroleum and natural gas are rapidly declining. Meanwhile, various multifunctional synthetic polymers are mainly produced from the depleted natural gas and petroleum. Furthermore, synthetic polymers are always difficult to be degraded, thus causing a severe white pollution. Therefore, polymer materials with good biocompatibility and degradable properties have attracted increased attention. Hydroxypropyl cellulose (HPC), belonging to nonionic cellulose ethers, is a semi-synthetic polymer material that is chemically modified from natural cellulose and exhibits nontoxicity, excellent biocompatibility, and biodegradability.¹ HPC has been widely considered to be an environmentally friendly and multifunctional polymer, which has been employed in the food-packaging, cosmetics, and biomedical fields.^{2–5}

Although pure polymer nanocomposite films are still far from being satisfactory for our daily life, it has been recognized that the performance could be significantly improved by introducing a low loading of nanofillers. For example, a composite polymer film could exhibit improved mechanical properties, ultraviolet (UV)–visible spectra, and antibacterial properties by filling a nanofiller into a polymer matrix.^{6–11} Specifically, Liu et al. prepared a novel poly(lactic acid)–graphene oxide (GO)–Ag hybrid nanocomposite fiber mat via electrospinning, and they demonstrated an enhanced bactericidal activity by filling 1 wt % GO–Ag (1–7 wt %) into the poly(lactic acid) (PLA) matrix.¹² Huang et al. prepared a

Received: May 5, 2019

Accepted: August 30, 2019

Published: September 11, 2019

multifunctional nanocomposite film with GO–ZnO (0.2–1 wt %) nanocomposites in the PLA matrix via solution blending.¹³ Moreover, the antibacterial activity of *E. coli* and *S. aureus* of the PLA/GO–ZnO nanocomposite films was clearly observed.^{13,14} Rehman et al. applied cornstarch cellulose nanocrystals in the presence of a low concentration of surfactants of sodium dodecyl sulfate or cetyltrimethylammonium bromide to fill the HPC matrix and obtained a bio-nanocomposite film with the uniform dispersion of nanocrystals, resulting in superior anti-UV and antibacterial properties.¹⁵

Recently, GO–inorganic nanocomposites have been investigated as fillers, and a series of excellent properties have been achieved.^{16–18} The considerable adhesion between GO and metal oxide nanomaterials is beneficial for applications involved charge transfer.¹⁹ However, the expected effect of GO–inorganic nanocomposites is limited when the content of inorganic nanofillers is small. In contrast, inorganic nanofillers would form agglomerates in the polymer matrix when increasing its amount to a certain degree.^{20–22} Therefore, it is critically important to find an approach to realize the desired impacts of nanofillers. Recently, GO with a large number of groups has been modified with isophorone diisocyanate (IPDI) (GO–IPDI) to further graft organic and inorganic nanoparticles to improve certain properties.^{23,24} For example, GOQD–IPDI–TA,²⁵ CuPc–g–GO,²⁶ GO–IPDI–MZ,²⁷ and GO–IPDI–CDs²⁸ have exhibited a range of unique and useful properties. Until now, only a few publications focus on polymer nanocomposite films with grafted nanomaterials as nanofillers.^{29,30} Ran et al. have reported a kind of GO–HA–AgNP nanocomposite film that is based on hyaluronidase (HAase)-triggered release to achieve effective antibacterial activity.³¹ The GO-based nanomaterials can raise the temperature locally, while the hyaluronic acid (HA) template can restrain AgNPs to protect mammalian cells. Other effective wound dressings include CiH-HMZS/P nanocomposite electrospun fibers designed by Zhang et al.,³² which can release Si ions locally to promote angiogenesis and skin regeneration and release zinc ions to enhance hair follicle regeneration as well as inhibit bacterial growth.

In this work, nanocomposite films were successfully prepared by a stepwise method.^{33,34} First, ZnO loaded with Ag nanoparticles (Ag/ZnO) was prepared. Then GO–IPDI–Ag/ZnO (AGO) nanocomposites were constructed thanks to the IPDI. Finally, AGO@HPC films were prepared through casting a mixed solution containing both HPC and AGO. The resulting AGO@HPC films exhibited enhanced mechanical, anti-UV, and antibacterial properties.

2. EXPERIMENTAL SECTION

2.1. Materials. All chemicals were of analytical grade. HPC (Klucel G Industrial) was purchased from Ashland Group. Zinc nitrate hexahydrate ($\text{Zn}(\text{NO}_3)_2 \cdot 6\text{H}_2\text{O}$, 99%) and silver nitrate (AgNO_3 , 99%) purchased from Guangzhou Chemical Reagents Co., Ltd. were used as raw materials to synthesize Ag/ZnO. Sodium hydroxide (NaOH), chloroform (CHCl_3), potassium permanganate (KMnO_4), and graphite powder were purchased from Tianjin Kemiou Chemical Reagent Co., Ltd. Sulfuric acid (H_2SO_4) and hydrogen peroxide (H_2O_2) were purchased from Guangzhou Chemical Reagents Co., Ltd. and Guangzhou Dongzheng Chemical Reagents Co., Ltd., respectively. Dibutyltin(II) dilaurate (97.5%) and IPDI (98%) were obtained from Thermo Fisher Scientific Co.,

Ltd. *N,N*-Dimethyl formamide (DMF) was supplied by Shanghai Runjie Chemical Reagent Co., Ltd.

2.2. Preparation and Modification of GO. GO was prepared from graphite flake powder through a modified Hummer's method according to a previous report.³⁵ Graphite powder (2 g) and P_2O_5 (2 g) were added to 46 mL of H_2SO_4 , and then they were stirred in an ice bath for 60 min. After 2 h, 6 g of KMnO_4 was gradually added to the solution while keeping the temperature less than 4 °C. The mixture was stirred at 35 °C for 2 h, and it was diluted by adding 200 mL of distilled water under strong stirring. The heating temperature was gradually raised to ~80 °C, and the mixture was maintained for 30 min before cooling to room temperature. The excess KMnO_4 was removed by the treatment with H_2O_2 , and it was washed several times with distilled water. GO was finally obtained by centrifugation at 10 000 rpm for 10 min and dried by freeze-drying. To prepare modified GO, 200 mg of the as-prepared GO was first dissolved in 50 mL of DMF and sonicated for 1.5 h. Then, 0.4 g of IPDI and 0.11 g of dibutyltin(II) dilaurate, which worked as catalysts, were introduced to the sonicated solution. After 24 h for the reaction under the condition of 50 °C (water bath) and nitrogen atmosphere protection, the suspension was washed with excess DMF to get rid of unreacted IPDI. Finally, the desired GO–IPDI was dried at 50 °C in a vacuum oven for 24 h.

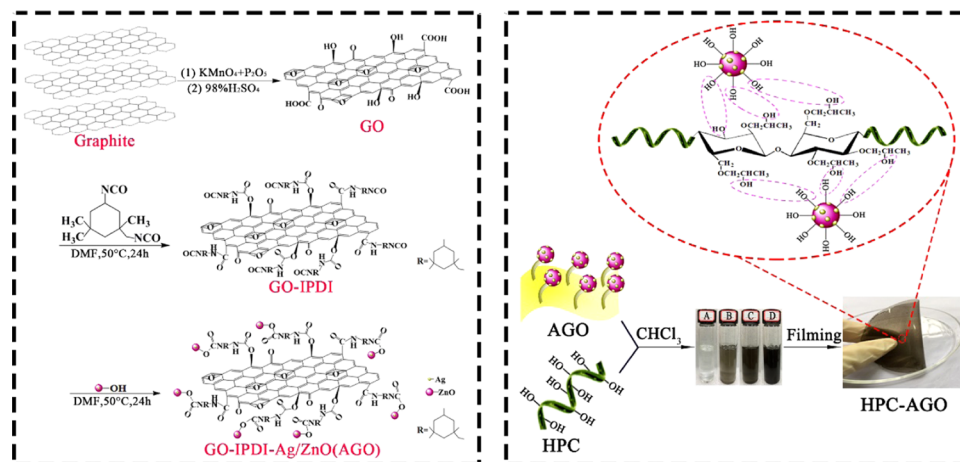
2.3. Synthesis of ZnO and Ag/ZnO Nanohybrid. Typically, 7.45 g of $\text{Zn}(\text{NO}_3)_2 \cdot 6\text{H}_2\text{O}$ was first dissolved in 50 mL of distilled water, and then 0.4 M NaOH solution was dropwise added into the above solution under vigorous stirring. The pH of the mixture was adjusted to 8–9 by NaOH solution. The mixture was continuously stirred at room temperature for 6 h. The obtained ZnO nanoparticles were washed with plenty of deionized water. Lastly, ZnO nanoparticles were filtered and dried at 60 °C for 24 h.

To prepare Ag/ZnO, 0.25 g of ZnO nanoparticles (NPs) was dispersed in 500 mL of deionized water in a three-necked flask and uniformly dispersed after the ultrasonic treatment. Then, 5 mL of 100 mM AgNO_3 was added, and they were sonicated for 30 min. The pH of the solution was adjusted to 8, and the solution was stirred in an oil bath at 80 °C for 5 h. After that, it was cooled down to room temperature and washed three times with deionized water and ethanol. The obtained Ag/ZnO was dried at 60 °C for 48 h in a vacuum oven. The silver loading in Ag/ZnO was ~6.13%.

2.4. Synthesis of GO–IPDI–Ag/ZnO. Briefly, 200 mg of GO–IPDI was immersed in 50 mL of DMF by ultrasonication in a dry nitrogen atmosphere for 1.5 h. Then, a certain amount of Ag/ZnO NPs (1, 2, and 5 wt %) was dispersed in 10 mL of anhydrous DMF for 1.5 h. Two suspensions were mixed and heated to 50 °C under stirring for 24 h in the presence of dibutyltin dicarboxylate. GO–IPDI–Ag/ZnO was washed at least three times with DMF and finally dried at 50 °C for 24 h in a vacuum oven.

2.5. Synthesis of AGO@HPC Composite Films. HPC (1 g) was dissolved in 16 mL of CHCl_3 and was stirred for 2 h. A certain amount of AGO (5 wt %) was dispersed in 4 mL of CHCl_3 and sonicated for 1.5 h. Then, AGO was added dropwise to the HPC-containing suspension and further stirred for 4 h at 50 °C. After that, the mixed suspension was dumped into a Petri dish. The solvent was evaporated at room temperature, and the AGO@HPC composite film with a thickness of ~100 μm was finally obtained after drying at 60

Scheme 1. Proposed Synthetic Route for AGO@HPC



°C for 48 h in vacuum. A proposed synthetic route for AGO@HPC is shown in Scheme 1.

2.6. Characterizations. X-ray diffraction (XRD) analysis was performed using a Blagg MSAL-XD2 (Beijing, China) instrument with a Cu K α radiation source (45 kV, 20 mA, and $\lambda = 0.15406$ nm). A 2θ range of $10\text{--}80^\circ$ was recorded in 0.02° steps at a rate of $2^\circ/\text{min}$. A Bruker (Germany) Vertex 70 Fourier transform infrared (FT-IR) spectrometer was used to perform the infrared analyses using the KBr pellet method. The spectra comprised 64 scans at a resolution of 1 cm^{-1} in the $4000\text{--}400\text{ cm}^{-1}$ spectral range. Thermogravimetric (TG) analyses were carried out using a Netzsch (Germany) 209 F1 thermogravimetric analyzer. About 5 mg of samples in sealed aluminum pans were analyzed under a nitrogen flow of 50 mL/min. Thermogravimetry analysis (TGA) curves and derivative thermogravimetry curves were recorded from room temperature to 600°C at a rate of $10^\circ\text{C}/\text{min}$. Scanning electron microscopy (SEM, ZEISS ULTRA 55) and transmission electron microscopy (TEM, JEM-2010 HR) were used to record the morphology, respectively, with accelerating voltages of 20 and 80 kV to study the morphology of the complex. Changes in the UV–visible spectra were monitored with a Shimadzu UV-2101PC spectrophotometer equipped with an integrating sphere.

2.7. Antibacterial Activity Evaluation. The antibacterial activity of the synthesized nanocomposite films were evaluated by the diameter of the inhibition zone on plates with solid-state nutrient agar against Gram-negative bacteria (*E. coli*) and Gram-positive bacteria (*S. aureus*). The nutrient broth (in tubes), nutrient agar (in flasks), and 0.85 wt % physiological saline (in flasks) were separately prepared and placed. The filled tubes and flasks were sealed with a piece of gauze and newspapers and further sterilized at 121°C in an autoclave for 15 min. Nutrient broth was further applied to incubate the bacteria, and it was put on a shaker for several days. The freshly grown bacterial solution (100 μL) was transferred to solid-state agar plates evenly. AGO@HPC composite films were laid on plates with solid-state nutrient agar in an incubator at 37°C for 1 day after the bacterial solution was completely diffused. Bear in mind, the whole process is carried out in a sterile environment. The diameter of the inhibition zone around the AGO@HPC composite film was measured at least three times. In addition, three replicates were performed under the same condition.

2.8. In Vivo Animal Experience. The male BALB/C mice (6 weeks) used in this experiment were provided by the Guangdong Medical Laboratory Animal Center. The mice were individually raised in cages for 1 week before animal experience. The temperature of animal cages is between 20 and 26°C , and the relative humidity is between 40 and 70%. All of the mice were divided into four groups (each group containing five mice): control group (treated by HPC), HPC–AGO-0.5 group (treated by HPC–AGO-0.5), HPC–AGO-1.0 group (treated by HPC–AGO-1.0), and HPC–AGO-2.0 group (treated by HPC–AGO-2.0), while every group has five mice. The mice were anesthetized by 6% chloral hydrate (0.45 mg/kg). We have built a wound model with a diameter of 6 mm on the back of each mouse surgically. Besides, the *S. aureus* (1.0×10^7 CFU/mL) was smeared on the thickness wounds. As the treatment beginning, each of the therapeutic dressings (such as HPC/HPC–AGO-0.5/HPC–AGO-1.0/HPC–AGO-2.0 described as before) was covered on the thickness wounds correspondingly. The dressings were changed every 2 days. Furthermore, the thickness wounds were observed and photographed. The skin tissues were sliced and stained with H&E and photographed by a microscope. The main organs like the heart, liver, spleen, lung, and kidney were sliced and stained with H&E after the 14 day treatment. The picture has been taken as described before.

3. RESULTS AND DISCUSSION

3.1. Structure and Morphology of Composite Materials. XRD patterns were recorded to check the possible structure evolution after composite formation. As shown in Figure 1a, the diffraction peak around $2\theta = 10.5^\circ$ can be indexed to the (002) plane of GO and the corresponding interlayer spacing is ~ 0.842 nm, indicating that the surface of GO is decorated with carboxyl and hydroxyl groups. The peak of GO is broadened and the average crystallinity is reduced compared with that of graphite carbon.³⁶ As can be seen from Figure 1b, a diffraction peak appears at $2\theta = 7.0^\circ$, and the corresponding layer spacing is ~ 1.263 nm. The shifts of GO–IPDI to a lower angle compared to that of the GO is mainly due to the intercalation between IPDI and GO layers. The introduction of IPDI increases the spacing of the GO interplanar layer. It also suggests that IPDI could play an important role in preventing graphene sheets from collapsing. As presented in Figure 1c, characteristic planes of both GO

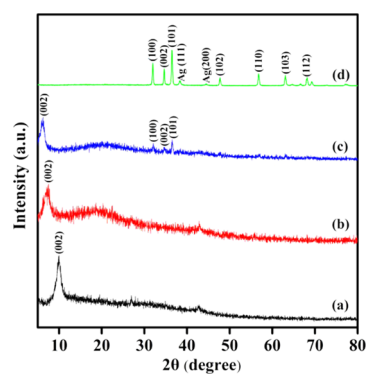


Figure 1. XRD patterns of GO (a), GO-IPDI (b), AGO (c), and Ag/ZnO (d).

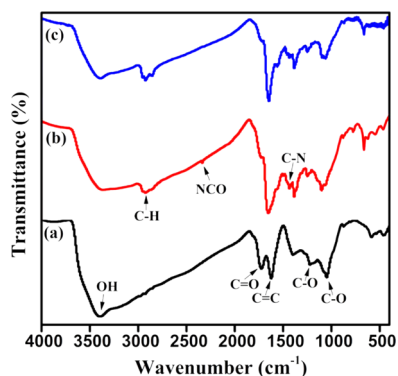


Figure 2. FT-IR spectra of GO (a), GO-IPDI (b), and AGO (c).

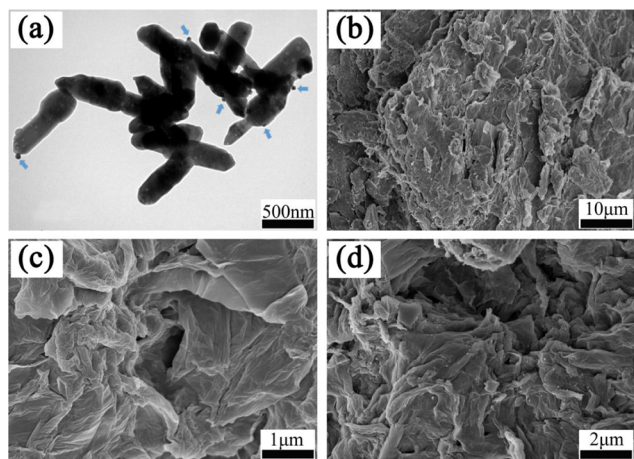


Figure 3. TEM image of Ag/ZnO (a), and SEM images of GO (b), GO-IPDI (c) and AGO (d).

and ZnO are clearly observed, indicative of the effective composite formation. The absence of Ag peaks is due to a low loading in Ag/ZnO. Anyway, Ag peaks of (111) and (200) planes can still be detected in Ag/ZnO (Figure 1d). Figure 1d also suggests that the ZnO is a hexagonal wurtzite structure,³⁷ and the corresponding planes are marked above the peak.

FT-IR was carried out to detect the possible evolution of the groups after composite formation. As shown in Figure 2a, the characteristic bands of 3395.9 cm^{-1} (OH), 1723.3 cm^{-1} (C=O), and 1621.6 cm^{-1} (C=C bond stretch) are clearly observed in GO. In addition, absorption peaks at 1223.0 and 1049.4 cm^{-1} correspond to stretching vibrations of epoxy (C-

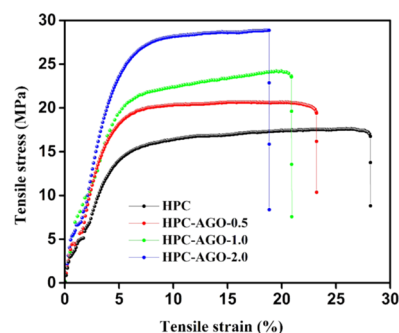


Figure 4. Tensile stress-strain curves of the pure HPC and AGO@HPC films.

Table 1. Tensile Strength and Elongation at Break of the Pure HPC and AGO@HPC Films

films	tensile strength (MPa)	elongation at break (%)
HPC	16.7 ± 0.3	28.2 ± 0.2
HPC-AGO-0.5	19.4 ± 0.2	23.2 ± 0.1
HPC-AGO-1.0	23.6 ± 0.3	20.9 ± 0.2
HPC-AGO-2.0	28.8 ± 0.1	18.9 ± 0.2

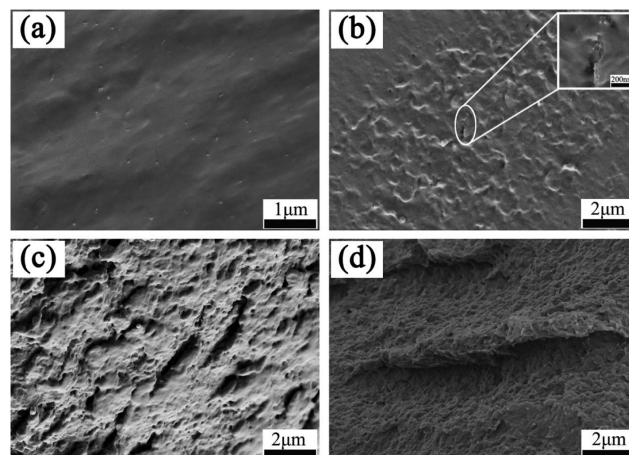


Figure 5. Cross-sectional SEM images of HPC (a), HPC-AGO-0.5 (b), HPC-AGO-1.0 (c), and HPC-AGO-2.0 (d).

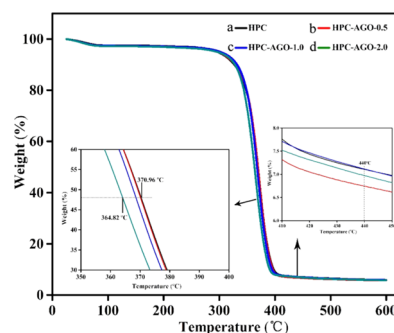


Figure 6. TG curves of pure HPC (a), HPC-AGO-0.5 (b), HPC-AGO-1.0 (c), and HPC-AGO-2.0 (d) at a heating rate of 10 $^{\circ}\text{C}/\text{min}$ in a nitrogen atmosphere.

OH) and alkoxy (C-O), respectively. For GO-IPDI, the C=O stretching vibration peak at 1723.3 cm^{-1} weakens, and new absorption peaks appear (Figure 2b). Absorption peaks at 1647.9 and 1435.3 cm^{-1} correspond to the stretching vibration peak of C-N in the carboxyl and carbamate in the amide. The

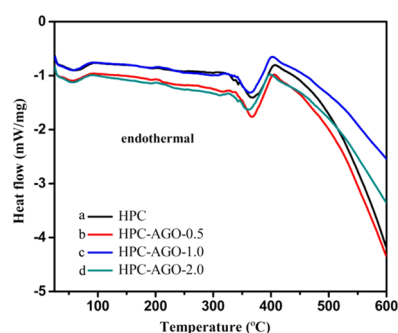


Figure 7. DSC curves of pure HPC (a), HPC–AGO-0.5 (b), HPC–AGO-1.0 (c), and HPC–AGO-2.0 (d) at a heating rate of 10 °C/min in a nitrogen atmosphere.

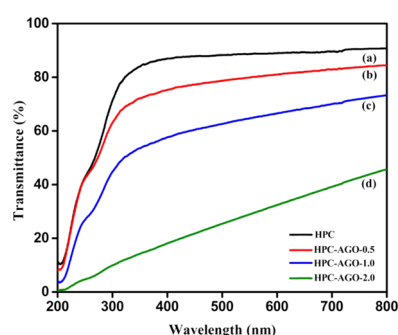


Figure 8. UV–vis transmittance spectra of HPC (a), HPC–AGO-0.5 (b), HPC–AGO-1.0 (c), and HPC–AGO-2.0 (d).

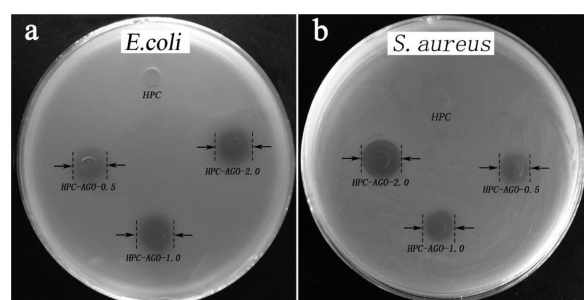


Figure 9. Photographs of agar plates cultivated with *E. coli* (a) and *S. aureus* (b), and the corresponding diameters of the inhibition zones formed by HPC, HPC–AGO-0.5, HPC–AGO-1.0, and HPC–AGO-2.0.

Table 2. Diameters of the Inhibition Zone of Pure HPC and AGO@HPC Films

films	diameter of the inhibition zone (mm)	
	<i>E. coli</i>	<i>S. aureus</i>
HPC	0	0
HPC–AGO-0.5	11.25 ± 0.45	12.18 ± 0.32
HPC–AGO-1.0	11.79 ± 0.39	12.71 ± 0.21
HPC–AGO-2.0	12.32 ± 0.65	13.76 ± 0.48

absorption peak at 2275–2363 cm^{-1} is attributed to the characteristic absorption peak of –NCO, indicating that a chemical reaction occurs when modifying GO with IPDI. As shown in Figure 2c, the characteristic peak of the isocyanate group disappears due to the chemical reaction between the isocyanate group and the hydroxyl group on the surface of ZnO.

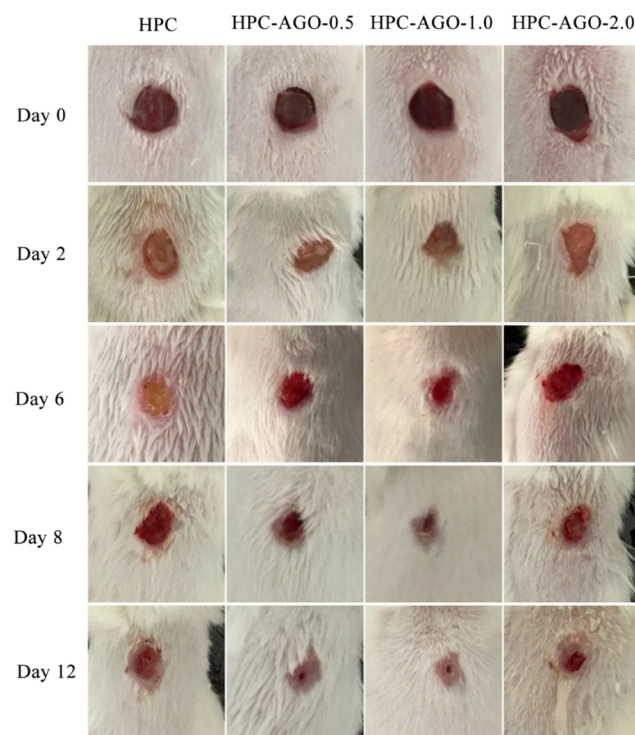


Figure 10. In vivo assessments of the curative effect-corresponding wound photographs.

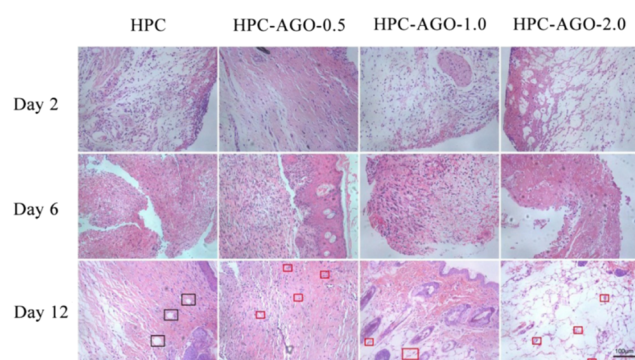


Figure 11. H&E staining of the skin tissue samples on rats' wounds after treatment. Scale bar, 100 μm .

The surface morphologies of Ag/ZnO, GO, GO–IPDI, and AGO were investigated by SEM and TEM. As shown in the TEM image (Figure 3a), Ag NPs are evenly loaded on the surface of ZnO. From the SEM images (Figure 3c,d), the surface morphology varies greatly. The surface of GO is randomly folded. After grafting of IPDI, the sheet structure is almost preserved, but it becomes more compact. In addition, wrinkles and curved edges appear, which is due to the covalent bonding between IPDI and GO. For AGO (Figure 3d), after grafting Ag/ZnO nanoparticles on the surface of GO–IPDI, it can be clearly seen that the surface of the sheet becomes more wrinkled because Ag/ZnO is well covalently grafted into the gap of GO–IPDI and evenly dispersed between its surface and between layers. In addition, some of the silver-loaded zinc oxide surface Ag NPs begin to detach from the surface and are uniformly dispersed on the fracture surface.

3.2. Mechanical, Thermal, Anti-UV, and Antibacterial Properties of Composite Films. Shown in Figure 4 and Table 1 are the stress–strain curve and the corresponding

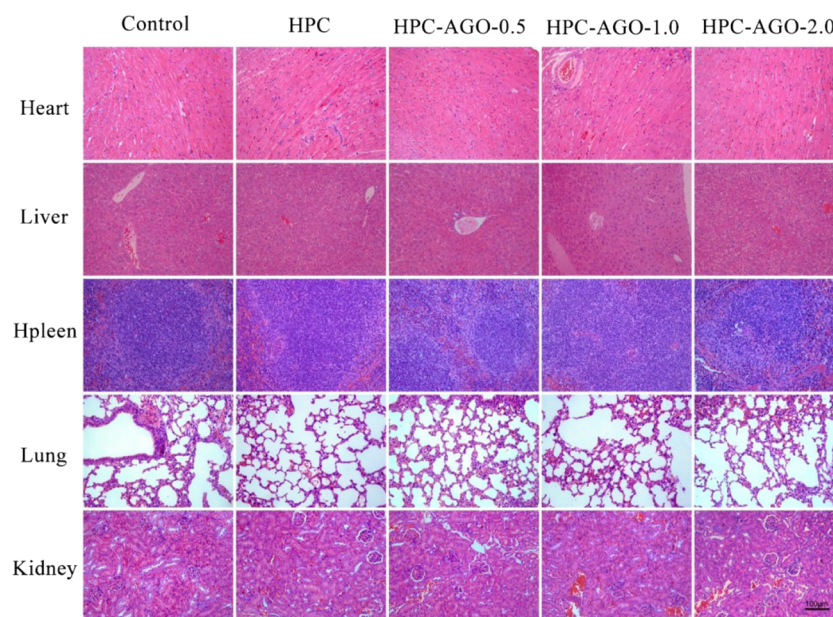


Figure 12. H&E staining of the heart, liver, spleen, lung, and kidney tissue slices after treatment. Scale bar, 100 μm .

tensile strength and elongation at break of HPC, HPC–AGO-0.5, HPC–AGO-1.0, and HPC–AGO-2.0. The tensile strength of the composite film is significantly increased with the incorporation of AGO, and it could be gradually increased by forming composites with an increased amount of AGO. Compared with the pure HPC film, the tensile strength of the composite film blended with 0.5 wt % AGO increased by $\sim 16.2\%$, indicating that the intercalation of AGO into the HPC matrix contributes greatly to the enhanced intermolecular interaction. The possible formation of increased physical or chemical cross-linking points thanks to the existence of surface hydroxyls is beneficial to improve mechanical properties.³⁸ Moreover, the tensile strength of HPC–AGO-2.0 increases by about 72.5%, which can be explained by the fact that the AGO sheet can be well-embedded in the HPC matrix, resulting in a strong interaction. In addition, the elongation at break of composite films is slightly reduced, which may slightly decrease the stretchability.

The cross-sectional microstructures of the pure HPC and AGO@HPC films are shown in Figure 5. The HPC film shows a smooth and uniform structure (Figure 5a). For the HPC–AGO-0.5 composite film (Figure 5b), a coarse structure can be clearly seen, which is due to the embedding of AGO into the HPC matrix. It is observed that the AGO composite is well-dispersed in the HPC matrix, which implies a good compatibility and a strong cross-linking between AGO and HPC. With the increase of the AGO content, the cross-sectional morphology of the composite films become more rough, and some nanoscaled pieces of AGO are pulled out. It may be due to fact that the gap between the fibrous HPC matrix is quite small, owing to which AGO tends to gather together.

Figure 6 shows TG curves of the pure HPC and HPC composite films. The thermal degradation process of all films can be divided into two stages. The weight loss in the first stage ($<100\text{ }^{\circ}\text{C}$) is about 3%, which is caused by the evaporation of residual water and organic solvents in the film. The second stage is at $240\text{--}440\text{ }^{\circ}\text{C}$ with a weight loss of up to $>90\%$, mainly due to the decomposition of HPC. Specifically,

the average decomposition temperature of the HPC–AGO-2.0 film is $364.8\text{ }^{\circ}\text{C}$ (enlarged view in the bottom left of Figure 6), which is a bit lower than that of pure HPC ($370.9\text{ }^{\circ}\text{C}$), indicating that the stability of the HPC film is slightly weakened due to the embedding of AGO. The carbon black yield of the AGO@HPC composite films reflected by the residual weight after $440\text{ }^{\circ}\text{C}$ is slightly lower than that of the pure HPC film, implying that there is an interaction between AGO and the HPC matrix, consistent with the above results.

To further analyze the stability of the pure HPC and HPC composite films, a differential scanning calorimetry (DSC) analysis was performed, as shown in Figure 7. Two endothermic peaks can be clearly observed, closely related to the stability of HPC. Endothermic peaks of HPC–AGO-0.5, HPC–AGO-1.0, and HPC–AGO-2.0 are at ~ 371.7 , 370.2 , and $367.3\text{ }^{\circ}\text{C}$, respectively, while the endothermic peak of pure HPC is at $\sim 372.0\text{ }^{\circ}\text{C}$, suggesting that the addition of AGO may slightly affect the thermal stability of HPC. However, we have to point out that the AGO@HPC composite films still maintain high stability.

Anti-UV properties of HPC and AGO@HPC films were determined by UV–visible spectroscopy, as shown in Figure 8. It can be clearly seen that pure HPC (Figure 8a) absorbs ultraviolet light ($200\text{--}400\text{ nm}$) but hardly absorbs visible light ($400\text{--}800\text{ nm}$), with a transmittance of about 90%. HPC–AGO-0.5 exhibits a certain UV resistance and a good visible light transmittance of about 84% (Figure 8b). With the increase of the AGO addition such as 1 wt % (Figure 8c) and 2 wt % (Figure 8d), the UV resistance is significantly improved. In particular, in the range of $200\text{--}800\text{ nm}$, HPC–AGO-2.0 shows quite a low light transmittance of about 45%, implying enhanced barrier properties. The enhanced anti-UV properties and the absence of additional peaks suggest the homogeneous dispersion of AGO in the HPC matrix.

Finally, antibacterial properties were systematically investigated. Gram-negative *E. coli* are one of the major categories of Enterobacteriaceae and are commonly found in the urinary tract and in the bloodstream as well as in the wound infection of hospital patients. *S. aureus* is a representative of Gram-

positive bacteria and can cause many serious infections, often resulting in a high morbidity and mortality. Therefore, Gram-negative bacteria (*E. coli*) and Gram-positive bacteria (*S. aureus*) were employed to check the antibacterial properties of HPC and AGO@HPC composite films.

The inhibition zones of HPC and AGO@HPC films against *E. coli* and *S. aureus* are shown in Figure 9. HPC does not show the bactericidal activity, but the addition of AGO to HPC inhibits the growth of *E. coli* and *S. aureus* to a certain extent. As listed in Table 2, the diameters of the inhibition zones of HPC-AGO-0.5, HPC-AGO-1.0, and HPC-AGO-2.0 for *E. coli* are 11.25 ± 0.45 , 11.79 ± 0.39 , and 12.32 ± 0.65 mm, while the inhibition zones for *S. aureus* are 12.18 ± 0.32 , 12.71 ± 0.21 , and 13.76 ± 0.48 mm. The antibacterial properties of AGO@HPC films increase with the addition of AGO. In addition, the diameters of the inhibition zones for *E. coli* and *S. aureus* are obviously different when adopting the same film, which may be caused by the different cell structures of bacteria.³⁹

The antibacterial mechanism is summarized as follows: (1) under the irradiation of a high energy, ZnO NPs can generate negatively charged electrons (e^-) and positively charged holes (h^+). e^- and h^+ can induce redox reactions on the surface of ZnO. h^+ can react with OH^- to generate hydroxyl radicals (OH^\bullet) on the surface of ZnO NPs as well as superoxide anions (O_2^-) and peroxy radicals (HO_2^\bullet).⁴⁰ These highly active free radicals can destroy the structure of microbial cells, thus exhibiting a bactericidal effect. (2) Zinc ions will be released when ZnO NPs come in contact with bacteria. The released zinc ions may penetrate the wall of the bacterial cell and may react with active proteases inside the bacteria.^{41,42} (3) In addition, Ag NPs exhibit effective bactericidal activity. Ag^+ can attach to the surface of bacterial cells, and disrupt its permeability and enter the cytoplasm, thus affecting the internal processes of cells and acting as a bactericidal agent.^{43,44} Moreover, the released Ag^+ can interact with the hydrophobic group of bacterial proteins to promote oxidative stress, which can cause damage to proteins and DNA, and further destroy the ability of DNA to replicate and kill bacteria.^{45–48} The diameter of the Ag NPs (1.44 Å) is significantly smaller than the diameter of the ZnO ions, thus making them easier to escape from the HPC matrix, anchoring on the surface and inside of the HPC matrix.^{29,49,50} In this work, Ag-loaded ZnO was grafted on the surface of GO, which provides a stable structure for the synergistic antibacterial activity. HPC was used as the matrix to make AGO embed and interact evenly, thus leading to the release of antibacterial substances with a long-acting antibacterial effect.

3.3. In Vivo Assessment of Wound-Healing. BALB/C mice have been used to build the skinny wound model. All of the animal models were divided into four groups: control group (treated by HPC, group I), HPC-AGO-0.5 group (treated by HPC-AGO-0.5, group II), HPC-AGO-1.0 group (treated by HPC-AGO-1.0, group III), and HPC-AGO-2.0 group (treated by HPC-AGO-2.0, group IV). The traumas were photographed on days 0, 4, 6, 8, and 12, as shown in Figure 10. Compared with group I, groups II, III, and IV show a smaller trauma size and less ichor after the 8 day treatment. Especially, the wounds in the control group on days 4 and 6 showed severe suppuration. After 12 days of treatment, the wounds of group II (treated by HPC-AGO-0.5) and group III (treated by HPC-AGO-1.0) showed significant healing. In general, the groups treated by AGO@HPC showed a better

curative effect, and the added AGO nanocomposite protected the body from bacterial infection.

The wound tissues on days 2, 6, and 12 were stained by hematoxylin and eosin (H&E). As shown in Figure 11, inflammatory reactions recruited a large number of neutrophils, which infiltrated the wound when bacterial infection occurred in vivo. With the process of wound-healing, newborn blood vessels (red rectangles) filled with a lot of red blood cells appeared in groups II, III, and IV. However, many necrotic foci (blank rectangles) have been observed in group I. Furthermore, the major organs (such as heart, liver, spleen, lung, and kidney) of mice were stained by hematoxylin and eosin (H&E). The results shown in Figure 12 do not indicate any damage effects after the treatment.

4. CONCLUSIONS

In this paper, multifunctional nanocomposite films composed of HPC and the AGO nanofillers were prepared by solution blending. XRD, FT-IR, and SEM results showed that the Ag/ZnO was successfully grafted on the GO surface, thus leading to the presence of the interaction between them. AGO nanocomposite materials were embedded and uniformly dispersed in the HPC matrix to form AGO@HPC films according the cross-sectional SEM images. The existence of a large number of hydroxyl groups led to a good mixing and a strong interaction between AGO and HPC. The tensile results suggested that the mechanical properties of AGO@HPC films were enhanced, while thermal measurements such as TG and DSC demonstrated that although decreased, the high stability of AGO@HPC films was still maintained. In addition, AGO@HPC nanocomposite films showed a strong UV resistance and could effectively inactivate both Gram-negative (*E. coli*) and Gram-positive (*S. aureus*) bacteria, and they also showed accelerated wound-healing. These effects could be further improved on further increasing the AGO content. Therefore, our results suggest that multifunctional AGO@HPC nanocomposite films with mechanical, anti-UV, and antibacterial properties could be applied in fields such as anti-UV treatment, antibacterial packaging, and biological wound-dressing.

AUTHOR INFORMATION

Corresponding Authors

*E-mail: tjzhy@jnu.edu.cn (Z.J.).

*E-mail: tsztan@jnu.edu.cn (S.T.).

ORCID

Dengjie Chen: 0000-0002-3234-7020

Shaozao Tan: 0000-0002-4669-0401

Author Contributions

^{||}Y.W. and L.S. contributed equally.

Notes

The authors declare no competing financial interest.

ACKNOWLEDGMENTS

This work was supported by grants from the National Natural Science Foundation of China (81473454, 51872124, and 21676116), the Science and Technology Projects of Guangdong Province (2016A010103020). This study also received assistance from the National science and technology major projects of China (2018ZX10715004-002), the Foshan Technology Research Center (2016GA10161), and the Project supported by GDHVPs (2017).

REFERENCES

- (1) Angelova, T.; Rangelova, N.; Yuryev, R.; Georgieva, N.; Müller, R. Antibacterial activity of SiO₂/hydroxypropyl cellulose hybrid materials containing silver nanoparticles. *Mater. Sci. Eng., C* **2012**, *32*, 1241–1246.
- (2) Angelova, T.; Rangelova, N.; Uzunova, V.; Georgieva, N.; Andreeva, T.; Momchilova, A.; Tzoneva, R.; Müller, R. Cytotoxicity and antibiofilm activity of SiO₂/cellulose derivative hybrid materials containing silver nanoparticles. *Turk. J. Biol.* **2016**, *40*, 1278–1288.
- (3) Ogiwara, T.; Katsumura, A.; Sugimura, K.; Teramoto, Y.; Nishio, Y. Calcium phosphate mineralization in cellulose derivative/poly (acrylic acid) composites having a chiral nematic mesomorphic structure. *Biomacromolecules* **2015**, *16*, 3959–3969.
- (4) Chiba, R.; Nishio, Y.; Sato, Y.; Ohtaki, M.; Miyashita, Y. Preparation of cholesteric (hydroxypropyl) cellulose/polymer networks and ion-mediated control of their optical properties. *Biomacromolecules* **2006**, *7*, 3076–3082.
- (5) El Fawal, G. F.; Abu-Serie, M. M.; Hassan, M. A.; Elnouby, M. S. Hydroxyethyl cellulose hydrogel for wound dressing: Fabrication, characterization and in vitro evaluation. *Int. J. Biol. Macromol.* **2018**, *111*, 649–659.
- (6) Moghimi, R.; Aliahmadi, A.; Rafati, H. Antibacterial hydroxypropyl methyl cellulose edible films containing nanoemulsions of *Thymus daenensis* essential oil for food packaging. *Carbohydr. Polym.* **2017**, *175*, 241–248.
- (7) Wang, Y.; Li, J.; Li, B. Nature-inspired one-step green procedure for enhancing the antibacterial and antioxidant behavior of a chitin film: controlled interfacial assembly of tannic acid onto a chitin film. *J. Agric. Food Chem.* **2016**, *64*, 5736–5741.
- (8) Jo, Y.; Choi, E.; Choi, N.; Kim, C. Antibacterial and hydrophilic characteristics of poly (ether sulfone) composite membranes containing zinc oxide nanoparticles grafted with hydrophilic polymers. *Ind. Eng. Chem. Res.* **2016**, *55*, 7801–7809.
- (9) Wang, X.; Zhu, S.; Liu, L.; Li, L. Flexible antibacterial film based on conjugated polyelectrolyte/silver nanocomposites. *ACS Appl. Mater. Interfaces* **2017**, *9*, 9051–9058.
- (10) Yang, Z.; Sun, C.; Wang, L.; Chen, H.; He, J.; Chen, Y. Novel Poly (l-lactide)/graphene oxide films with improved mechanical flexibility and antibacterial activity. *J. Colloid Interface Sci.* **2017**, *507*, 344–352.
- (11) Wang, L.; Li, J.; Zhang, S.; Shi, J. Preparation and characterization of all-biomass soy protein isolate-based films enhanced by epoxy castor oil acid sodium and hydroxypropyl cellulose. *Materials* **2016**, *9*, 193.
- (12) Liu, C.; Shen, J.; Yeung, K. W. K.; Tjong, S. C. Development and antibacterial performance of novel polylactic acid-graphene oxide-silver nanoparticle hybrid nanocomposite mats prepared by electrospinning. *ACS Biomater. Sci. Eng.* **2017**, *3*, 471–486.
- (13) Huang, Y.; Wang, T.; Zhao, X.; Wang, X.; Zhou, L.; Yang, Y.; Liao, F.; Ju, Y. Poly (lactic acid)/graphene oxide–ZnO nanocomposite films with good mechanical, dynamic mechanical, anti-UV and antibacterial properties. *J. Appl. Chem. Biotechnol.* **2015**, *90*, 1677–1684.
- (14) Adeli, H.; Khorasani, M. T.; Parvazinia, M. Wound dressing based on electrospun PVA/chitosan/starch nanofibrous mats: Fabrication, antibacterial and cytocompatibility evaluation and in vitro healing assay. *Int. J. Biol. Macromol.* **2019**, *122*, 238–254.
- (15) Rehman, N.; de Miranda, M. I. G.; Rosa, S. M.; Bica, C. I. Reinforcement of hydroxypropylcellulose films by cellulose nanocrystals in the presence of surfactants. *Chin. J. Polym. Sci.* **2016**, *34*, 1301–1310.
- (16) Govindhan, P.; Pragathiswaran, C.; Chinnadurai, M. Facile synthesis of GO/ZnO–Ag nanocomposite and evaluation of rhodamine B dye under sun light. *J. Mater. Sci.: Mater. Electron.* **2017**, *28*, 354–362.
- (17) Zhang, H.-Z.; Zhang, C.; Zeng, G.-M.; Gong, J.-L.; Ou, X.-M.; Huan, S.-Y. Easily separated silver nanoparticle-decorated magnetic graphene oxide: synthesis and high antibacterial activity. *J. Colloid Interface Sci.* **2016**, *471*, 94–102.
- (18) Pant, B.; Saud, P. S.; Park, M.; Park, S.-J.; Kim, H.-Y. General one-pot strategy to prepare Ag–TiO₂ decorated reduced graphene oxide nanocomposites for chemical and biological disinfectant. *J. Alloys Compd.* **2016**, *671*, 51–59.
- (19) Bai, S.; Shen, X. Graphene–inorganic nanocomposites. *RSC Adv.* **2012**, *2*, 64–98.
- (20) Ojha, D. P.; Joshi, M. K.; Kim, H. J. Photo-Fenton degradation of organic pollutants using a zinc oxide decorated iron oxide/reduced graphene oxide nanocomposite. *Ceram. Int.* **2017**, *43*, 1290–1297.
- (21) Perdikaki, A.; Galeou, A.; Pilatos, G.; Karatasios, I.; Kanellopoulos, N. K.; Prombona, A.; Karanikolos, G. N. Ag and Cu monometallic and Ag/Cu bimetallic nanoparticle–graphene composites with enhanced antibacterial performance. *ACS Appl. Mater. Interfaces* **2016**, *8*, 27498–27510.
- (22) Dubey, P.; Gopinath, P. PEGylated graphene oxide-based nanocomposite-grafted chitosan/polyvinyl alcohol nanofiber as an advanced antibacterial wound dressing. *RSC Adv.* **2016**, *6*, 69103–69116.
- (23) Zhang, P.; Gong, J.-L.; Zeng, G.-M.; Deng, C.-H.; Yang, H.-C.; Liu, H.-Y.; Huan, S.-Y. Cross-linking to prepare composite graphene oxide-framework membranes with high-flux for dyes and heavy metal ions removal. *Chem. Eng. J.* **2017**, *322*, 657–666.
- (24) Sun, L.; Du, T.; Hu, C.; Chen, J.; Lu, J.; Lu, Z.; Han, H. Antibacterial activity of graphene oxide/g-C₃N₄ composite through photocatalytic disinfection under visible light. *ACS Sustainable Chem. Eng.* **2017**, *5*, 8693–8701.
- (25) Zhang, C.; Wei, K.; Zhang, W.; Bai, Y.; Sun, Y.; Gu, J. Graphene oxide quantum dots incorporated into a thin film nanocomposite membrane with high flux and antifouling properties for low-pressure nanofiltration. *ACS Appl. Mater. Interfaces* **2017**, *9*, 11082–11094.
- (26) Wang, Z.; Wei, R.; Liu, X. Preparation and dielectric properties of copper phthalocyanine/graphene oxide nanohybrids via in situ polymerization. *J. Mater. Sci.* **2016**, *51*, 4682–4690.
- (27) Lei, L.; Shan, J.; Hu, J.; Liu, X.; Zhao, J.; Tong, Z. Co-curing effect of imidazole grafting graphene oxide synthesized by one-pot method to reinforce epoxy nanocomposites. *Compos. Sci. Technol.* **2016**, *128*, 161–168.
- (28) Yan, J.; Zhu, Y.; Qiu, F.; Zhao, H.; Yang, D.; Wang, J.; Wen, W. Kinetic, isotherm and thermodynamic studies for removal of methyl orange using a novel β -cyclodextrin functionalized graphene oxide-isophorone diisocyanate composites. *Chem. Eng. Res. Des.* **2016**, *106*, 168–177.
- (29) Mahdavi, H.; Rahmani, O.; Shahverdi, A. R. Polyacrylamide/reduced graphene oxide-Ag nanocomposite as highly efficient antibacterial transparent film. *J. Iran. Chem. Soc.* **2017**, *14*, 37–46.
- (30) Tsai, Y.-H.; Yang, Y.-N.; Ho, Y.-C.; Tsai, M.-L.; Mi, F.-L. Drug release and antioxidant/antibacterial activities of silymarin-zein nanoparticle/bacterial cellulose nanofiber composite films. *Carbohydr. Polym.* **2018**, *180*, 286–296.
- (31) Ran, X.; Du, Y.; Wang, Z.; Wang, H.; Pu, F.; Ren, J.; Qu, X. Hyaluronic acid-templated Ag nanoparticles/graphene oxide composites for synergistic therapy of bacteria infection. *ACS Appl. Mater. Interfaces* **2017**, *9*, 19717–19724.
- (32) Zhang, Y.; Chang, M.; Bao, F.; Xing, M.; Wang, E.; Xu, Q.; Huan, Z.; Guo, F.; Chang, J. Multifunctional Zn doped hollow mesoporous silica/polycaprolactone electrospun membranes with enhanced hair follicle regeneration and antibacterial activity for wound healing. *Nanoscale* **2019**, *11*, 6315.
- (33) Fu, F.; Gu, J.; Cao, J.; Shen, R.; Liu, H.; Zhang, Y.; Liu, X.; Zhou, J. Reduction of Silver Ions Using an Alkaline Cellulose Dope: Straightforward Access to Ag/ZnO Decorated Cellulose Nanocomposite Film with Enhanced Antibacterial Activities. *ACS Sustainable Chem. Eng.* **2018**, *6*, 738–748.
- (34) Al Aani, S.; Gomez, V.; Wright, C. J.; Hilal, N. Fabrication of antibacterial mixed matrix nanocomposite membranes using hybrid nanostructure of silver coated multi-walled carbon nanotubes. *Chem. Eng. J.* **2017**, *326*, 721–736.

- (35) Hummers, W. S., Jr.; Offeman, R. E. Preparation of graphitic oxide. *J. Am. Chem. Soc.* **1958**, *80*, 1339.
- (36) Ko, Y. C.; Fang, H. Y.; Chen, D. H. Fabrication of Ag/ZnO/reduced graphene oxide nanocomposite for SERS detection and multiway killing of bacteria. *J. Alloys Compd.* **2017**, *695*, 1145–1153.
- (37) Abinaya, C.; Marikkannan, M.; Manikandan, M.; Mayandi, J.; Suresh, P.; Shanmugaiah, V.; Ekstrum, C.; Pearce, J. M. Structural and optical characterization and efficacy of hydrothermal synthesized Cu and Ag doped zinc oxide nanoplate bactericides. *Mater. Chem. Phys.* **2016**, *184*, 172–182.
- (38) Díez-Pascual, A. M.; Díez-Vicente, A. L. ZnO-reinforced poly (3-hydroxybutyrate-co-3-hydroxyvalerate) bionanocomposites with antimicrobial function for food packaging. *ACS Appl. Mater. Interfaces* **2014**, *6*, 9822–9834.
- (39) van der Wal, A.; Norde, W.; Zehnder, A. J.; Lyklema, J. Determination of the total charge in the cell walls of Gram-positive bacteria. *Colloids Surf., B* **1997**, *9*, 81–100.
- (40) Liu, Y.; Morishima, T.; Yatsui, T.; Kawazoe, T.; Ohtsu, M. Size control of sol–gel-synthesized ZnO quantum dots using photo-induced desorption. *Nanotechnology* **2011**, *22*, No. 215605.
- (41) Liu, Y.; Kim, H.-I. Characterization and antibacterial properties of genipin-crosslinked chitosan/poly (ethylene glycol)/ZnO/Ag nanocomposites. *Carbohydr. Polym.* **2012**, *89*, 111–116.
- (42) Li, Z.; Zhang, F.; Meng, A.; Xie, C.; Xing, J. ZnO/Ag micro/nanospheres with enhanced photocatalytic and antibacterial properties synthesized by a novel continuous synthesis method. *RSC Adv.* **2015**, *5*, 612–620.
- (43) Gogoi, S. K.; Gopinath, P.; Paul, A.; Ramesh, A.; Ghosh, S. S.; Chattopadhyay, A. Green Fluorescent Protein-Expressing *Escherichia coli* as a Model System for Investigating the Antimicrobial Activities of Silver Nanoparticles. *Langmuir* **2006**, *22*, 9322–9328.
- (44) Sun, X.-F.; Qin, J.; Xia, P.-F.; Guo, B.-B.; Yang, C.-M.; Song, C.; Wang, S.-G. Graphene oxide–silver nanoparticle membrane for biofouling control and water purification. *Chem. Eng. J.* **2015**, *281*, 53–59.
- (45) Shao, W.; Liu, X.; Min, H.; Dong, G.; Feng, Q.; Zuo, S. Preparation, characterization, and antibacterial activity of silver nanoparticle-decorated graphene oxide nanocomposite. *ACS Appl. Mater. Interfaces* **2015**, *7*, 6966–6973.
- (46) Whitehead, K.; Vaidya, M.; Liauw, C.; Brownson, D.; Ramalingam, P.; Kamieniak, J.; Rowley-Neale, S.; Tetlow, L.; Wilson-Nieuwenhuis, J.; Brown, D.; McBain, A. J. Antimicrobial activity of graphene oxide-metal hybrids. *Int. Biodeterior. Biodegrad.* **2017**, *123*, 182–190.
- (47) Matsumura, Y.; Yoshikata, K.; Kunisaki, S.-i.; Tsuchido, T. Mode of bactericidal action of silver zeolite and its comparison with that of silver nitrate. *Appl. Environ. Microbiol.* **2003**, *69*, 4278–4281.
- (48) Dashdorj, U.; Reyes, M. K.; Unnithan, A. R.; Tiwari, A. P.; Tumurbaatar, B.; Park, C. H.; Kim, C. S. Fabrication and characterization of electrospun zein/Ag nanocomposite mats for wound dressing applications. *Int. J. Biol. Macromol.* **2015**, *80*, 1–7.
- (49) Ravichandran, K.; Uma, R.; Sriram, S.; Balamurgan, D. Fabrication of ZnO: Ag/GO composite thin films for enhanced photocatalytic activity. *Ceram. Int.* **2017**, *43*, 10041–10051.
- (50) Ghosh, S.; Goudar, V.; Padmalekha, K.; Bhat, S.; Indi, S.; Vasan, H. ZnO/Ag nanohybrid: synthesis, characterization, synergistic antibacterial activity and its mechanism. *RSC Adv.* **2012**, *2*, 930–940.